INL/JOU-16-40252-Revision-0

Lanthana-bearing nanostructured ferritic steels via spark plasma sintering

James I. Cole, Sultan F. Alsagabi, Somayeh Pasebani, Indrajit Charit, Yaqiao Wu, Jatuporn Burns, Kerry N. Allahar, Darryl P. Butt

March 2016

The INL is a U.S. Department of Energy National Laboratory
operated by Battelle Energy Alliance

INL/JOU-16-40252-Revision-0

Lanthana-bearing nanostructured ferritic steels via spark plasma sintering

James I. Cole, Sultan F. Alsagabi, Somayeh Pasebani, Indrajit Charit, Yaqiao Wu, Jatuporn Burns, Kerry N. Allahar, Darryl P. Butt

March 2016

Idaho National Laboratory
Idaho Falls, Idaho 83415

http://www.inl.gov

Prepared for the
U.S. Department of Energy
Office of Nuclear Energy
Under DOE Idaho Operations Office
Contract DE-AC07-05ID14517

Lanthana-bearing nanostructured ferritic steels via spark plasma sintering

Somayeh Pasebani[a,d], Indrajit Charit[a,d,1] , Yaqiao Wu[b,d], Jatuporn Burns[b,d], Kerry N. Allahar[b,d], Darryl P. Butt[b,d], James I. Cole[c,d], Sultan F. Alsagabi[a,d]

[a] Department of Chemical and Materials Engineering, University of Idaho, Moscow, ID 83844, USA

[b] Department of Materials Science and Engineering, Boise State University, Boise, ID 83725, USA

[c] Idaho National Laboratory, Idaho Falls, ID 83401, USA

[d] Center for Advanced Energy Studies, Idaho Falls, ID 83401, USA

Abstract

A lanthana-containing nanostructured ferritic steel (NFS) was processed via mechanical alloying (MA) of Fe-14Cr-1Ti-0.3Mo-0.5La_2O_3 (wt.%) and consolidated via spark plasma sintering (SPS). In order to study the consolidation behavior via SPS, sintering temperature and dwell time were correlated with microstructure, density, microhardness and shear yield strength of the sintered specimens. A bimodal grain size distribution including both micron-sized and nano-sized grains was observed in the microstructure of specimens sintered at 850, 950 and 1050 ^{o}C for 45 min. Significant densification occurred at temperatures greater than 950 ^{o}C with a relative density higher than 98%. A variety of nanoparticles, some enriched in Fe and Cr oxides and copious nanoparticles smaller than 10 nm with faceted morphology and enriched in La and Ti oxides were observed. After SPS at 950 ^{o}C, the number density of Cr-Ti-La-O enriched nanoclusters with an average radius of 1.5 nm was estimated to be 1.2 $\times 10^{24}$ m^3. The La + Ti : O ratio was close to 1 after SPS at 950 and 1050 ^{o}C; however, the number density of nanoclusters decreased at 1050 ^{o}C. With SPS above 950 ^{o}C, the density improved but the microhardness and shear yield strength decreased due to partial coarsening of the grains and nanoparticles.

Keywords**:** *mechanical alloying; powder metallurgy; sintering; steels; nanostructured materials; atom probe*

[1] Corresponding author (I. Charit): e-mail: icharit@uidaho.edu; phone: +1-208-885-5964; fax: +1-208-885-7462

1. Introduction

Nanostructured ferritic steels (NFSs) are considered potential candidates for fuel cladding and structural applications in advanced nuclear reactors. These steels possess high creep and tensile strength combined with excellent radiation damage tolerance [1-3]. The NFSs are distinguished from conventional oxide dispersion strengthened (ODS) steels because of the finer microstructure and smaller size of oxide dispersions. The unique properties of some of the NFSs such as 12YWT (Fe-12Cr-3W-0.4Ti-0.25Y_2O_3, wt.%) and 14YWT (Fe-14Cr-2W-0.3Ti-0.3Y_2O_3, wt.%) are derived from the presence of an ultrahigh density of Y-Ti-O-enriched NCs. These NCs are formed via MA of Fe-Cr-Ti powder with Y_2O_3 followed by a hot consolidation route [4-6].

The most commonly used Rare Earth (RE) oxide in ferritic ODS or NFSs is yttria (Y_2O_3). In the present study, the potential of using an alternative RE oxide in processing a new NFS was investigated by replacing the Y_2O_3 with lanthanum oxide (La_2O_3). This replacement can be rationalized based on various favorable characteristics of lanthana such as high temperature stability [7], lower diffusion rate and negligible solubility of lanthanum in iron in solid state [8], relative abundance of lanthanum in common rare earth based ores, and evidence of enhancing mechanical properties in other BCC-based alloy (molybdenum) systems [9,10].

In this study, La_2O_3 (0.5 wt.%) was added to Fe-14Cr-1Ti-0.3Mo (wt.%) powder mix, to produce an alloy composition with approximately equal atomic fraction of Y_2O_3 present in commercially produced MA957 alloy (Fe-14Cr-1Ti-0.3Mo-0.3Y_2O_3, wt.%). The NFS with nominal composition of Fe-14Cr-1Ti-0.3Mo-0.5La_2O_3 (wt.%) is termed as 14LMT, hereafter. In addition to resorting to alternative RE addition, spark plasma sintering (SPS) was used as a consolidation method following mechanical alloying in place of other traditional consolidation methods such as hot extrusion and hot isostatic pressing (HIP). Compared to hot extrusion and HIP, the SPS technique allows sintering at lower temperatures and shorter dwell times. In SPS, the powder mixture is uniaxially pressed similar to hot pressing while a DC pulse voltage is applied to the compact simultaneously. While in the case of electrically conductive materials, heating is mainly due to the Joule effect, the understanding of the SPS process is still evolving [11-13].

There have been only a limited number of studies on the application of SPS in consolidating the ODS steels and NFSs [9,14-19]. A detailed account of the mechanically alloyed 14LMT powder was presented in our previous studies [20, 21] and revealed the presence of NCs in the nanocrystalline ferritic matrix after mechanical alloying, The effect of alloying elements and milling time on the microstructure and hardness is reported elsewhere [9, 22]. The present study focuses on understanding the effects of two SPS parameters, temperature and dwell time, on the microstructural evolution including grain size and grain structure, particle and matrix composition, size and number density of nanoprecipitates as well as mechanical properties of 14LMT alloy.

2. Experimental Procedures

2.1. Material and Processing Methods

The starting constituent powders including Fe (99.9 wt.%, average particle size of 40 μm), Cr (99.8 wt.%, average particle size of 5 μm), Ti (99.7 wt.%, average particle size of 26 μm), La_2O_3 (99.99 wt.%, average particle size of 40 nm) and Mo (99.9 wt.%, average particle size of 1-2 μm) were mixed in the nominal proportion of Fe-14Cr-1Ti-0.3Mo-0.5La_2O_3 (wt.%). Except for Mo powder that was acquired from the Micron Metal Powder Inc., the rest of powders were procured from the American Elements Inc. High energy ball milling was performed in an air-cooled SPEX 8000M mixer/mill for 10 h using Thompson 52100 chrome steel balls with ~8 mm diameter as the milling media. A milling batch consisted of 100 g steel balls and 10 g powder giving a ball to powder ratio (BPR) of 10:1. A Dr. Sinter Lab SPS-515S machine (SPS Syntex Inc., Kanagawa, Japan) was used to consolidate the as-milled powder. A Tri-Gemini cylindrical graphite die with an inner diameter of 12.7 mm and an outer diameter of 38 mm was used. In order to inhibit the diffusion of carbon from the punches and graphite foil to the powder mixture, a thin niobium foil was placed between the powder and the graphite foils. The die was wrapped in a graphite felt (4 mm in thickness) to minimize heat loss by thermal radiation. The as-milled powder was sintered under vacuum (7×10^{-3} Torr or 0.9 Pa) at temperatures of 850, 950 and 1050 ^{o}C and various dwell times of 0, 2, 7, 20 and 45 min. A pulsed DC current with pattern of 12-2 (current on for 12 ms and off

for 2 ms), a heating rate of 100 ºC/min and a pressure of about 80 MPa were used. The temperature was monitored with a K-type thermocouple that was inserted in a hole in the die such that the tip was located 6 mm away from the sintering powder. The sintered samples were cooled to room temperature in the vacuum chamber at about 50 ºC/min. The final product was in the form of a disk with 12.5 mm diameter. The temperature, applied current, voltage, applied pressure and vertical displacement of the lower punch were monitored and recorded during the sintering process.

2.2. Microstructural and Compositional Characterization

X-ray diffraction (XRD) of the as-milled powders was performed using a Siemens 5000D diffractometer with Cu K_α radiation (wavelength 0.15406 nm). The crystallite size and lattice strain were calculated using the Williamson–Hall method using the data presented in Ref. [21]. Microstructural characteristics of the sintered specimens were examined using a Zeiss LEO Supra 35 VP FESEM at accelerating voltages of 15-20 kV. Some specimens were also prepared for electron back-scatter diffraction (EBSD) characterization by polishing sequentially from 120 through 1200 grit SiC papers, followed by a final polish in a Buehler Vibromet-2 vibratory polisher using 0.05 μm alumina slurry for 6 to 24 h. The EBSD analysis was performed on a JEOL JSM-6610LV scanning electron microscope (SEM) equipped with an EDAX/TSL Hikari EBSD system. The SEM was operated at an accelerating voltage of 20 kV. The automated scan was performed with a 0.1 μm step size on a total area of 50×50 μm^2. The EBSD data were analyzed using the TSL Orientation Imaging Microscopy (OIM™) Data Collection version 5.31 software. After SPS, disks with 3 mm in diameter were mechanically thinned and electropolished in an electrolyte of CH_3OH-HNO_3 (80:20 by vol.%) at a temperature of -30 ºC using a Fischione Model 110 Twin-Jet Electropolisher. Transmission electron microscopy (TEM) studies along with energy dispersive spectroscopy (EDS) experiments were performed using a FEI Tecnai TF30 FEG STEM operating at 300 kV. A focused ion beam (FIB) available in a FEI Quanta 3D FEG instrument with a Ga-ion source was used to prepare specimens for atom probe tomography (APT) studies. The APT analysis was carried out using a CAMECA LEAP 4000X HR operating in voltage mode at the specimen temperature of 50–60 K

and 20% of the standing voltage pulse fraction. The atom maps were reconstructed using CAMECA IVAS 3.6 software. The maximum separation cluster algorithm was used to identify the composition of NCs. The maximum separation between solute atoms is defined as d_{max} whereas L is the maximum separation of additional elements, $N_{\min}$ is the minimum size of a cluster and E is the erosion distance for removal of atoms near the cluster/matrix interface. An N_{min} value of 10-15, d_{max} values of 0.6-0.8 nm, L values of 0.4-0.5 nm and E values ranging from 0.3-0.5 nm were chosen based on procedures described comprehensively in the literature [6, 22-25]. The bulk composition was calculated based on the total number of atoms of each element in a complete analysis volume and was averaged over at least three different tip coupons. A background noise correction was applied to the mass spectrum and the matrix composition was calculated by excluding those atoms defined as a cluster based on the maximum separation method. The size of NCs was estimated from the radius of gyration (R_g) that is the average distance between each atom and center of a corresponding cluster [26, 27]. This was applied to APT datasets each containing 20-30 million ions. The clustering of each individual oxide-type was investigated, and Ti-O, Cr-O along with La showed clustering (according to the reduced Chi square (χ^2) values) [27]. The quantity of matrix was artificially set to zero using a model outlined by Williams *et al.* [6] in order to remove the matrix contribution. The cluster composition calculated this way was termed "matrix corrected " [6].

2.3. Evaluation of Density and Mechanical Properties

The density of the sintered specimens was measured by Archimedes' method. At least six measurements were made for each specimen. The final relative density was expressed in percentage and determined as the ratio between the measured and the theoretical density (~7.7 g/cm^3) of 14LMT alloy. The Vickers microhardness tests were performed using a Leco LM100 microhardness tester at a 1 kg (9.81 N) with a dwell time of 15 s.

Shear punch experiments were carried out on an Instron 5967 electromechanical test frame. Several shear-punch disk specimens with 3 mm in diameter were punched out from the foils with an average thickness of 250-350 μm. Tests were conducted at room temperature using a displacement rate of

240 μm/min and repeated three to four times for each processing condition. The shear punch fixture included a 1 mm diameter flat-end punch, which sheared a portion of a 3 mm diameter specimen into a 1.02 mm diameter hole in the receiving die. Punch displacement was measured using a linear variable differential transformer (LVDT) with a range of ±3.2 mm. Shear punch data were obtained in terms of the punch load and displacement. Then the shear yield strength was determined using the following equation:

$$\tau = \frac{p}{2\pi rt} \qquad (1)$$

where p is the load, r is the average of the hole and punch radii, and t is the specimen thickness [28].

3. Results

3.1. Effect of the SPS temperature and time on the microstructural evolution

3.1.1. SEM and EBSD studies

Figs. 1a-c show SEM micrographs along with corresponding EBSD maps as insets from various 14LMT specimens SPSed at 850, 950 and 1050 ^{o}C for 45 min, respectively. The EBSD micrograph inside Fig. 1a revealed bimodal grain size distribution with a combination of nanograins and coarse grains (in fact ultrafine grains) in the consolidated microstructure. The proportion of coarser grains increased at the expense of nanograins with increasing sintering temperature as shown in Figs. 1b and c.

The porosity in Fig. 1 was revealed as regions with dark contrast. Overall, the volume fraction of porosity was found to decrease with increasing SPS temperature. The porosity volume fraction was calculated to be 6.4±2.3% and 5.1±2.1% after SPS at 850 ^{o}C for 7 and 45 min, respectively. Increasing the dwell time from 7 min to 45 min at 950 ^{o}C improved densification to some extent with the porosity fraction decreasing from 1.1±0.3% to 0.8±0.3%. The porosity fraction in Fig. 1c was estimated to be 0.7±0.2%. Higher SPS temperature improved densification to a noticeable extent in the alloy but was accompanied by a higher proportion of coarse grains. Furthermore, it is evident that the main densification process occurred at 950 ^{o}C, above which the porosity was almost eliminated.

3.1.2. TEM studies

TEM bright field images of the overall grain structure and nanoparticles present in the 14LMT alloy specimen sintered at 850 ^{o}C for 45 min are shown in Figs. 2a and b. A non-uniform distribution of ultrafine grains with a broad grain size distribution (~ 100 nm to 1 μm) and nanograins (< 100 nm) can be observed as revealed in Fig. 2a. The type of non-homogeneous distribution of grains is quite similar to the bimodal grain size distribution observed in other studies [14, 17]. Boundaries of the ultrafine grains were pinned by either large nanoparticles or by the triple-junction of the grain boundaries themselves. The presence of the particles on the boundaries and interior of the ultrafine grains imply that these particles had a significant role in controlling dynamic recrystallization and subsequent microstructural evolution. The average diameter of nanograins and ultrafine grains in the 14LMT alloy specimen after SPS at 850 ^{o}C for 45 min was measured to be 76±10 nm and 470±30 nm, respectively. The proportion of ultrafine grains was approximately 37% with the rest as nanograins. Particles with diameter between 2-30 nm were observed as shown in Fig. 2b. Further EDS analysis (not shown here) demonstrated that these faceted nanoparticles contained La and Ti along with matrix elements and oxygen. The microstructure of the 14LMT alloy sintered at 950 ^{o}C for 45 min is shown in Figs. 2c and d. The bimodal distribution of nano and ultrafine grains was revealed in Fig. 2c. The microstructure contained a high number of dislocations along with nanoparticles and nanograins. The recrystallized ultrafine grains were surrounded by the nanograins and non-uniformly distributed across the microstructure. The average diameter of nanograins and ultrafine grains in this 14LMT specimen was calculated to be 112±10 nm and 539±30 nm, respectively. Approximately 45% of the area contained the ultrafine grains.

The microstructure of the 14LMT alloy specimen sintered at 1050 ^{o}C for 45 min is shown in Figs. 2e and f. The area fraction of recrystallized grains was estimated to be approximately 60%. The average diameter of nanograins and ultrafine grains in the 14LMT alloy after SPS at 1050 ^{o}C for 45 min was calculated to be 154±15 nm and 785±60 nm, respectively. The micrograph, shown in Fig. 2e revealed a high number density of nanoparticles interacting with dislocations inside a large grain. The HRTEM

image shown in Fig. 2f revealed the oxide particles with a diameter in the range of 2-5 nm. The increased SPS temperature (1050 ^{o}C) did not cause any significant coarsening of nanoparticles, specifically those that were smaller than 5 nm.

Four particles with faceted morphology and an average diameter smaller than 10 nm are highlighted in the HAADF STEM image of Fig. 3a with a scan line running across them. The corresponding EDS line-scan profile is plotted in Fig. 3b. It shows that the Ti and La were mostly concentrated in the particles rather than the ferritic matrix. The EDS analyses indicated that the concentration of Cr, Ti and La varied within the particles and particle/matrix interface. There was a wide diversity between the particles in terms of size, morphology and chemical composition.

The EFTEM (energy-filtered TEM) elemental composition micrographs from the particles are presented in Figs. 4a-f. In Fig. 4a, the signals from the Fe-$L_{2,3}$ peak became weaker in the particles and showed darker contrast identifying less iron content in the particles. However, the larger particles were found to be somewhat enriched in chromium as shown in Fig. 4b. In Fig. 4c, Ti was clearly distinguishable in particles while Mo revealed darker contrast in the EFTEM map shown in Fig. 4d meaning of no Mo were found in the particles. In EDS results, larger particles did not contain any La, and similarly in EFTEM elemental map in Fig. 4e no La enrichment was observed in larger particles. It was difficult to obtain an EFTEM image from 2-3 nm diameter particles due to relatively large thickness of the specimen and large excitation volume. Therefore, La mapping could not be clearly realized in smaller particles, as shown in Fig. 4e, due to insufficient sensitivity, low spatial resolution and low signal to noise ratio. The particles contained oxygen as shown in Fig. 4f. However, the oxygen in the smaller particles could not be unambiguously revealed likely because oxygen was already present on the sample surface. The EFTEM maps in Fig. 4a-f implies the presence of Cr, Ti and O in the particles. Despite the absence of La in the larger particles in EFTEM maps, its presence in the smallest particles also could not be clearly resolved using EFTEM. The particle size distribution plots of 14LMT alloy after SPS at 850, 950 and 1050 ^{o}C for 45 min are shown in Fig. 5. In order to construct the plots Approximately 1,000 particles were counted from several TEM micrographs for each SPS condition. The percentage of particles with

diameters smaller than 5 nm was estimated to be 83%, 64% and 50% at the SPS temperatures of 850, 950 and 1050 ^{o}C, respectively. Greater number of coarse particles were obtained at higher SPS temperatures. The number of 5-10 nm particles was higher at the SPS temperature of 950 ^{o}C than at 850 ^{o}C and at 1050 ^{o}C, whereas the proportion of particles larger than 10 nm was higher at 1050 ^{o}C than at the other two SPS temperatures.

3.1.3. APT results

Figure 6 illustrates the distribution of solutes in a small volume (18×18×50 nm^3) of the 14LMT alloy specimen (sintered at 950 ^{o}C for 45 min). It revealed clustering of Cr-, Ti-, La- and O-enriched particles. The presence of Cr and Ti ions in the form of oxide ions is due to their strong affinity for O. The O atoms showed a broader distribution than TiO and La likely due to the irregular oxygen evaporation from the tip [25]. Most Mo atoms were distributed uniformly throughout the matrix. The bulk composition, matrix average composition, cluster average composition and matrix-corrected composition are calculated and summarized in Table 1. The cluster composition was calculated using the maximum separation algorithm [29]. Here core atoms of La, O and TiO were selected using a maximum separation distance (d_{max}) of 0.6-0.8 nm, and clusters were found to be composed of at least 10 core atoms (N_{min} = 10-15) within d_{max}.

The number density of Cr-, Ti-, La-, O-enriched NCs in 14LMT alloy sintered at 950 ^{o}C for 45 min was estimated to be 1.2×10^{24} m^{-3} with a (Guinier) radius of 1.5±0.3 nm. The average cluster composition was 9±2 at.% Cr, 18±2 at.% Ti, 6±1 at.% La, 35.2±3 at.% O along with Fe as the balance. The matrix-corrected cluster composition indicated that the particles were enriched in Cr, Ti, La and O and was depleted in Mo and Fe with a stoichiometry of (La+Ti):O being about 0.98. The effect of SPS temperature on the distribution, chemical composition and nanocluster size was studied by conducting APT analyses on the 14LMT alloy sintered at 1050 ^{o}C for 45 min. The corresponding 3D-APT maps are shown in Fig. 7. The Cr-, Ti-, La-, O-enriched NCs with an average (Guinier) radius of 2.0±0.2 nm and a number density of 6.6×10^{23} m^{-3} were detected in thisspecimen. With increasing SPS temperature, the NCs became only slightly larger in size and less in number but did not bear any significant change. The

average cluster composition was found to be 14±1 at.% Cr, 23±3 at.% Ti, 11±0.5 at.% La, 30.0±5 at.% O along with Fe as the balance. The matrix-corrected cluster composition indicated that the particles were indeed enriched in Cr, Ti, La and O and depleted in Mo and Fe with a stoichiometry of (La+Ti):O being 1.03.

3.2. Density and mechanical properties

In order to study the combined effect of SPS temperature and time, the three temperatures (850, 950 and 1050 ^{o}C) were selected, and the dwell time was varied between 0 and 45 min isothermally. The density and microhardness values were measured and presented in Figs. 8a and b, respectively. The relative density of the sintered specimens increased with increasing SPS temperature from 850 to 1050 ^{o}C at all dwell times. The relative density values did not change significantly after 20 min at 850 ^{o}C and after 7 min at 950 and 1050 ^{o}C. The relative density values after SPS at 850, 950 and 1050 ^{o}C for 45 min were 94.3%, 97.8% and 98.3%, respectively. Microhardness of the 14LMT specimens sintered at 850 and 950 ^{o}C increased consistently with increasing dwell time from 0 to 45 min. However, the microhardness decreased after SPS at 1050 ^{o}C beyond 2 min dwell time. The microhardness values were 489, 561 and 324 HV, after SPS at 850, 950 and 1050 ^{o}C for 45 min, respectively. The shear yield stresses of the 14LMT alloys processed for two different sintering times (7 and 45 min) and three temperatures are included in Fig. 8c. A 0.01 offset shear strain was used to calculate the shear yield stress in the punch displacement traces [30, 31]. The shear yield stress values were higher for 14LMT alloys processed at 950 ^{o}C for 7 and 45 min than those processed at 850 and 1050 ^{o}C. The shear yield stress revealed a similar trend to microhardness of the same materials.

4. Discussion

4.1. Microstructural evolution

Most of the mechanically alloyed powders are composed of non-equilibrium phase constituents with a very large amount of stored energy. Formation of a supersaturated solid solution consisting of Cr,

Ti, La, O and Mo in a ferritic matrix via high energy ball milling of elemental powders practically occurs when the powder particles become fragmented and smaller until eventually disappearing into a super saturated solid solution. This can be done by inducing an immense quantity of dislocations as well as vacancies that actually act as "*solute-pumping stations*" to introduce solutes (here Cr, Ti, Mo and La) into the crystalline lattices [32]. As ball milling proceeds, the interfacial energy increases with the refinement of the powder particles providing a sufficient driving force for any recrystallization and second phase precipitation during further consolidation [33]. Often during consolidation, the mechanically alloyed powder may recrystallize to a sub-micron grain size which is representative of the grain structure found immediately after consolidation [34]. The presence of nano and ultrafine grains in bimodal grain structured observed in Figs. 2 and 3 is attributed to partial recrystallization facilitated in some regions with higher dislocation densities such as in the vicinity of larger Cr-Fe oxide particles, or prior grain or crystallite boundaries. The high number of nanoparticles in the microstructure can have a complex effect on the recrystallization process through Zener pinning [35]. The partial recrystallization can be explained by applying a model initially proposed by Bhadeshia [34]. In this model, grain junctions act as the pinning points during the formation of nuclei and thus retard recrystallization. With this model, it is plausible that the nucleation of recrystallized grains shown in Fig. 2c occurred through formation of grain boundary bulges, as grain junctions were the pinning points making it difficult for bulge nuclei to grow further [34]. Furthermore, at 950 ^{o}C, the recrystallization rate was controlled by a high number density of nanoparticles as shown in Fig. 2d. Recrystallization process gets hindered in the presence of nanoparticles as long as $F_v/r > 0.2$ μm^{-1} where F_v is the volume fraction of particles and r is the particle radius [35]. In the SPSed material, F_v/r is larger than 0.2 μm^{-1} if we use 0.0055 for the F_v and 35-40 nm in diameter for the particles. Residual pores for example as visible in Fig. 1b, may also play a role in pinning boundaries and hindering the recrystallization process [35]. Sub-grains shown in Fig. 2e were formed by the rearrangement of dislocations and controlled by nanoparticles. Meanwhile, due to recovery in these grains, the driving force for recrystallization would possibly no longer be sufficient and further recrystallization initiation would be delayed.

Allahar *et al.* [14] reported the development of a similar bimodal grain size distribution in the SPSed Fe-16Cr-3Al-0.5Y_2O_3-1Ti (wt.%) ODS alloy. It was also attributed to the occurrence of partial recrystallization. Boulant *et al.* [36] implied that the heterogeneous plastic deformation which is characteristic of any high energy ball milling process is the main reason of a heterogeneous recrystallization or abnormal grain growth during sintering.

By adjusting alloying elements and processing parameters, it is possible to control the distribution of the oxide particles grain size in NFSs to a relatively optimized condition. In conventional sintering process such as HIP or hot extrusion, due to the higher operating temperatures and indirect heating of the non-equilibrium powder, recrystallization is likely to be completed before the precipitation occurs and therefore the particles will not have a great influence on the recrystallization process. On the other hand, in SPS a lower sintering temperature and shorter dwell time would not cause significant coarsening in nanoparticles that have already nucleated during milling [18] and get solute-enriched during sintering. This can enhance the influence of nanoparticles on the grain structure at higher temperature once the primary consolidated microstructure formed during recovery and subsequent recrystallization. Although nanoparticles smaller than 5 nm did not significantly coarsen at 1050 ^oC as shown in Fig. 2f, the number of these particles was noticeably reduced at the higher SPS temperature. The fraction of the nanoparticles smaller than 5 nm was estimated to be 83%, 64% and 50% at 850, 950 and 1050 ^oC, respectively (Fig. 5). The lower fraction of the smaller particles and coarsening of the particles at higher SPS temperature likely facilitated recrystallization at 1050 ^oC. To summarize the microstructural evolution during sintering of the milled powder in SPS process, a hypothesis is suggested; a supersaturated milled powder with nano-crystalline domains with high number of vacancies, dislocations and grain boundaries, vacancies-O atoms pairs [37], has a very high amount of stored energy for a possible fast recovery process to form sub-grains. During sintering, vacancies annihilation, thermal vacancies generation, dislocations recovery and sub-grain formation lead to recrystallized nuclei, recovered grains and formation of precipitates. For example; after SPS at 850 ^oC, nanograins with the smallest nano-oxide precipitates were observed along with recrystallized ultrafine grains with larger precipitates. Although the precipitation formation and

recrystallization are two competing processes, there is not enough evidence which one occurs earlier if they are not occurring simultaneously. However, it is more likely true that recrystallization will be more dominant than precipitation formation at higher SPS temperature (e.g. 1050 ^{o}C) due to higher mobility of grain boundaries and coarsening of the oxide nanoprecipitates.

The APT maps in Figs. 6-7 showed that NCs in this alloy are non-stoichiometric and Cr, Ti-, La and O- enriched. In order for NCs to nucleate during ball milling, a super saturated solid solution has to be formed first. This meta-stable state can be achieved by continuous particle shearing and thermally activated jumps. The numerous O-vacancies pairs are created in a ball-milled Fe system and attract atoms with high affinity for O such as Cr, Ti and La [38]. Nucleation of Y–O [6] and similarly La-O can be facilitated by the presence of Cr and Ti in part of the oxide clusters. The nucleation of a high number density of Cr-, Ti-, La-, O-enriched NCs have been formerly reported in the ball milled 14LMT ferritic matrix [21]. Despite more negative enthalpy of La-O formation the initial oxides were Cr- and Ti- based due to the higher concentration of O, Cr and Ti, larger La atoms and lower diffusion rate of La in the Fe lattice.

During initial stages of consolidation, remaining vacancies and dislocations created from milling, along with thermally activated vacancies and excess vacancies induced by different diffusion rates of solutes are presumed to greatly enhance nanocluster formation through a fast vacancy-based diffusion mechanism. Nevertheless, Brocq *et al*. [38] have reported that at 800 ^{o}C, most of the milling-generated vacancies were annihilated in a Fe-based matrix and further nucleation of NCs did not happen. In 14LMT alloy system, the atomic radius of La (195 pm) is greater than that of Y (180 pm), and thus a greater misfit is introduced into the bcc ferritic matrix and the formation of NCs with interfacial phases such as TiO and CrO are preferred. Hence, the oxidation kinetics will result in the formation of Cr–O and Ti–O, which may assist in further nucleation of La–O [39].

With increasing SPS temperature from 950 ^{o}C to 1050 ^{o}C, the number density of NCs decreased to almost 50% but the R_G increased. A higher SPS temperature could provide more thermally activated vacancies in the Fe-based system and compensate for the large misfit of La-O by rapid diffusion of

solute-vacancy pair. This is likely the reason for the higher La content in composition of NCs at higher SPS temperatures.

4.2. Mechanical properties

A high hardness (561 HVN) was achieved in 14LMT alloy after SPS at 950 °C for 45 min that can be attributed to the following strengthening contributions: (1) precipitation strengthening from the RE oxide particles such as La_2O_3 particles and the presence of the Ti-Cr-rich phase, (2) grain boundary strengthening due to grain refinement (Hall-Petch relationship), (3) solid solution strengthening and (4) dislocation strengthening [40]. Thus, the yield strength (σ_y) can be given by the following relation:

$$\sigma_y = \sigma_o + \sigma_s + \sigma_d + \sigma_{GB} + \sigma_p \qquad (2)$$

where σ_o is the friction stress representing the minimum resistance of the crystal lattice to dislocation movement (28 MPa for interstitial-free iron) [17], σ_s is the solid solution strengthening, σ_d is the dislocation strengthening, σ_{GB} is grain boundary strengthening, and σ_p is the particle strengthening. Although no tensile yield values were reported in this study, the shear yield stresses are included in Fig. 8c.

Toloczko *et al.* [30] have shown that the shear punch traces can be compared to the corresponding tensile traces by considering that in a shear punch test reduction in load bearing area is increasingly controlled by cutting of the material as the punch displacement becomes large. Thus, for materials which display low uniform elongation, the reduction in loading area is probably most strongly controlled by the same processes which control it in a tensile test.

For polycrystalline specimens, the uniaxial tensile stress is related to the critical resolved shear stress by the Taylor factor (M):

$$\sigma = M \times \tau \qquad (3)$$

where M equals 2.7 for BCC metals [41]. Since the average shear yield value of 14LMT alloy SPSed at 950 °C was measured to be 392 MPa, a rough estimation for tensile yield would be 1058 MPa.

The strength of material can be improved by addition of solutes to the matrix by introducing a strain field due to the atomic misfit. The nominal composition of the present alloy is Fe-14Cr-1Ti-0.3Mo-0.5La_2O_3 (wt.%). Solid solution strengthening contributions due to the addition of chromium and molybdenum has only been considered since most of Ti and La are present in the oxide particles based on the TEM and APT results. The solid solution strengthening contribution can be expressed as:

$$\sigma_{ss} = \sum AC_i \qquad (4)$$

where C_i is the element concentration in wt.% and A is a coefficient. For Cr, Mo and C or N, A is equal to 8.5, 57.9, and 5544 MPa/(wt.%), respectively, in ferritic steels [42, 43]. The carbon and nitrogen content in the matrix solid solution came from the milling media and were unavoidable. The resulting contribution from the solid solution strengthening was estimated to be 190 MPa.

In a bimodal grain size distribution, σ_{GB} can be expressed by [17]:

$$\sigma_{GB} = k\left[(1 - V_f)\, D_{nano}^{-0.5} + V_f\, D_{coarse}^{-0.5}\right] \qquad (5)$$

where k is the Hall-Petch constant, V_f is the volume fraction of coarse-grained region, and D_{nano} and D_{coarse} are the average size of the nanograins (here 110 nm) and coarse grains (here 850 nm), respectively. The grain boundary contribution is calculated by assuming the Hall-Petch relation is valid and is a single constant for the observed nano grain size range. The constant k was estimated to be 260 MPa $\mu m^{0.5}$ [17], and the value for σ_{GB} is roughly estimated to be 328 MPa.

The precipitation hardening contribution [17] can be expressed as:

$$\sigma_p = k'\lambda_s^{-0.5} \qquad (6)$$

$$\lambda_s = 1.22\{[\pi/(4f_v)]^{0.5} - 1\}d \qquad (7)$$

where λ_s is the surface to surface interparticle spacing, k' is a constant (roughly estimated to be 395 MPa $\mu m^{0.5}$), f_v is the volume fraction of oxide particles and d is the average diameter of oxide particles. The σ_p is roughly estimated to be 450 MPa by having 0.0055 for the f_v, and 35-40 nm for d in the equation. The contribution of dislocation strengthening was estimated to be 62 MPa. From the preceding calculations, it

is clear that almost 42% of the yield strength comes from due to the precipitation hardening effect and , the contribution of solid solution strengthening and grain boundary strengthening were roughly 18% and 31%, respectively, and the rest is comprised of dislocation strengthening and friction stress.

5. Conclusions

In this study, the potential use of an alternative RE oxide in processing a NFS was investigated by adding 0.5 wt.% La_2O_3 to Fe-14Cr-1Ti-0.3Mo (wt.%). The mechanically alloyed powder was consolidated via SPS at 850, 950 and 1050 ^oC with a dwell time of 0 to 45 min. The influence of sintering parameters such as sintering temperature and dwell time on the microstructure, density, microhardness and shear yield strength was investigated. After sintering, a bimodal grain size distribution consisting of micronsized and nanometric grains were observed in the microstructure. Main densification occurred at 950 ^oC which improved with longer dwell time. Hence, the optimum sintering condition was found to be 950 ^oC for 45 min. Oxide nanoparticles formed before and during SPS impede any grain growth in the sintered specimens. The average size of these oxide particles was smaller than 5 nm. However, particle coarsening was observed after sintering at 1050 C. The APT analysis of the specimen sintered at 950 ^oC revealed high number density of 1.2×10^{24} m^3 of NCs with the average radius of 1.5 nm, enriched in Cr, Ti, La and O. The La + Ti:O ratio was close to 1. At 1050 ^oC, the number density of NCs decreased to 0.66×10^{24} m^3 and the average radius increased slightly. The presence of high number of NCs along with the Hall-Petch strengthening mechanism, dislocation hardening and solid solution hardening led to significant hardening observed in these alloys. While the 14LMT alloy has showed promise as a potential alternative to yttria-containing NFSs, further in-depth studies are needed to understand all the issues involving this novel alloy.

Acknowledgments

This work was supported partly by the Laboratory Directed Research and Development Program of Idaho National Laboratory (INL), Contract DE-AC07-05ID14517, and partly by a grant (# 15- 543-RTE) of the Nuclear Science User Facility (NSUF). The authors greatly acknowledge staff of the

Microscopy and Characterization Suite (MaCS) facility at the Center for Advanced Energy Studies (CAES), Idaho Falls, USA. We would also like to thank the reviewers for their helpful comments and suggestions.

References

[1] Y. Wu, E.M. Haney, N.J. Cunningham, G.R. Odette, Acta Mater. 60 (2012) 3456-3468.

[2] H. Kishimoto, M.J. Alinger, G.R. Odette, T. Yamamoto, J. Nucl. Mater. 329-333 (2004) 369-371.

[3] G.R. Odette, M.L. Alinger, B.D. Wirth, Annu. Rev. Mater. Res. 38 (2008) 471-503.

[4] S. Ukai, T. Okuda, M. Fujiwara, T. Kobayashi, S. Mizuta, H. Nakashima. J. Nucl. Sci. Tech. 39 (2002) 872-879.

[5] S. Ukai, M. Fujiwara, J. Nucl. Mater. 307-311 (2002) 749-757.

[6] C.A. Williams, P. Unifantowicz, N. Baluc, G.D.W. Smith, E.A. Marquis, Acta Mater. 61 (2013) 2219-2235.

[7] ASM Handbook, ASM International, 3rd ed., Materials Park (OH), 1992

[8] Z.D. Reed, M.A. Duncan, J. Phys. Chem. 112 (2008) 5354-5362.

[9] S. Pasebani, I. Charit, J. Alloys Compd. 599 (2014) 206-211.

[10] A.J. Mueller, R. Bianco, R.W. Buckman, Int. J. Refract. Met. Hard Mater. 18 (2000) 205-211.

[11] R.S. Mishra, A.K. Mukherjee, K. Yamazaki, K. Shoda, J. Mater. Res. 11 (1996) 1144-1148.

[12] M. Gendre, A. Maitre, G. Trolliard, Acta Mater. 58 (2010) 2598-2609.

[13] A.M. Locci, R. Orru, G. Cao, Z.A. Munir, Mater. Sci. Eng. A 434 (2006) 23-29.

[14] K.N. Allahar, J. Burns, B. Jaques, Y.Q. Wu, I. Charit, J. Cole, DP Butt, J. Nucl. Mater. 443 (2013) 256-265.

[15] Y.Q. Wu, K.N. Allahar, J. Burns, B. Jaques, I. Charit, D.P. Butt, J.I. Cole, Cryst. Res. Technol. (2013) DOI 10.1002/crat.201300173:1-8.

[16] W.S. Young, I.B. Cutler. J. Am. Ceram. Soc. 53 (1970) 659-663.

[17] B. Srinivasarao, K. Ohishi, T. Ohkubo, K. Hono, Acta Mater. 57 (2009) 3277-3286.

[18] C. Heintze, A.H. Mayoral, A. Ulbricht, F. Bergner, A. Shariq, T. Weissgarber, H. Frielinghaus, J. Nucl. Mater. 428 (2012) 139-146.

[19] C. Heintze, F. Bergner, A. Ulbricht, M. Hernandez, U. Keiderling, R. Lindau, T. Weissgarber, J. Nucl. Mater. 416 (2011) 35-39.

[20] S. Pasebani, I. Charit, D.P. Butt, J.I. Cole, J. Nucl. Mater. 434 (2013) 282-286.

[21] S. Pasebani, I. Charit, D.P. Butt, J.I. Cole, Acta Mater. 61 (2013) 5605-5617.

[22] D. Vaumousse, A. Cerezo, P.J. Warren, Ultramicroscopy 95 (2003) 215-221.

[23] T. Leigh, M.P. Moody, P.V. Liddicoat, S.P. Ringer, Microsc. Microanal. 13 (2007) 448-463.

[24] A. Cerezo, L. Davin, Surf. Interface Anal. 39 (2007) 184-188.

[25] C.A. Williams, E.A. Marquis, A. Cerezo, G.D.W. Smith, J. Nucl. Mater. 400 (2010) 37-45.

[26] M.K. Miller, Atom Probe Tomography, Kluwer Academic/ Plenum, New York, 2000.

[27] C.A. Williams, D. Haley, E.A. Marquis, G.D. Smith, M.P. Moody, Ultramicroscopy 132 (2013) 271-278.

[28] G.L. Hankin, M.B. Toloczko, M.L. Hamilton, R.G. Faulkner, J. Nucl. Mater. 1651 (1998) 258-263.

[29] L.T. Stephenson, M.P. Moody, P.V. Liddicoat, S.P. Ringer, Microsc. Microanal. 13 (2007) 448-463.

[30] M.B. Toloczko, R.J. Kurtz, A. Hasegawa, K. Abe, J. Nucl. Mater. 307-311 (2002) 1619-1623.

[31] V. Karthik, P. Visweswaran, A. Vijayraghavan, K.V. Kasiviswanathan, B. Raj, J. Nucl. Mater. 393 (2009) 425-432.

[32] A.Y. Badmos, H.K.D.H. Bhadeshia, Metall. Mater. Trans. A 28 (1997) 2189-2194.

[33] L.M. Brocq, F. Legendre, M.H. Mathon, A. Mascaro, S. Poissonnet, B. Radiguet, P. Pareige, M. Loyer, O. Leseigneur, Acta Mater. 60 (2012) 7150-7159.

[34] H.K.D.H. Bhadeshia, Mater Sci Eng A 223 (1997) 64-77.

[35] F.J. Humphreys, M. Hatherly, Recrystallization and Related Phenomena, Pergamon, London, 1995.

[36] X. Boulant, M. Perez, D. Fabregue, T. Douillard, M.H. Mathon, Y.D. Carlan, Metall. Mater. Trans. A 45A (2014) 1485-1497.

[37] C.L. Fu, M. Kremar, G.S. Painter, Physc. Rev. Lett. 99 (2007) 225502-225504.

[38] L.M. Brocq, B. Radiguet, S. Poissonnet, F. Cuvilly, P. Pareige, F. Legendre, J. Nucl. Mater. 409 (2011) 80-85.

[39] M.K. Miller, D.T. Hoelzer, E.A. Kenik, K.F. Russell, J Nucl. Mater. 329-333 (2004) 338-333.

[40] R. Song, D. Ponge, D. Raabe, Scripta Mater. 52 (2005) 1075-1080.

[41] U.F. Kocks, Metall. Mater. Trans. A 1 (1970) 1121-1143.

[42] J. Wang, W. Yuan, R.S. Mishra, I. Charit, J. Nucl. Mater. 432 (2013) 274-280.

[43] G.E. Totten, L. Xie, K. Funatani, Handbook of Mechanical Alloy Design, CRC Press, New York, 2003.

Table 1. Composition measurements based on the APT data obtained from 14LMT alloy after SPS at 950 °C for 45 min

Element	Compositional measurements			
	Bulk (at.%)	Matrix (at.%)	Cluster (at.%)	Matrix- corrected (at.%)
Cr	13.88±0.5	10.73±0.3	8.9±2.2	31.82±3.2
O	0.39±0.1	0.12±0.06	35.25±3.2	34.2±4.3
Ti	1.09±0.09	0.25±0.1	17.8±2.0	25.5±2.1
C	0.1±0.05	0.10±0.05	0.05±0.04	0.09±0.05
N	0.09±0.04	0.10±0.05	0.04±0.02	0.04±0.05
La	0.14±0.06	0.05±0.04	7.89±0.84	10.31±0.1
Mo	0.17±0.05	0.16±0.05	0.06±0.03	0.04±0.04
Fe	84.14±0.5	88.49±0.3	32.01±6.4	0.0

Table 2. Composition measurements based on the APT data obtained from 14LMT alloy after SPS at 1050 °C for 45 min

Element	Compositional measurements			
	Bulk (at.%)	Matrix (at.%)	Cluster (at.%)	Matrix-corrected (at.%)
Cr	14.56±0.7	11.12±0.5	14.14±1.2	15.4±3.3
O	0.45±0.1	0.15±0.06	30.0±5.5	41.63±2.5
Ti	0.9±0.2	0.12±0.1	23.3±3.1	27.77±0.5
C	0.12±0.05	0.08±0.06	0.05±0.03	0.05±0.05
N	0.10±0.04	0.08±0.05	0.04±0.04	0.02±0.02
La	0.16±0.05	0.05±0.05	11.1±0.5	15.11±1.5
Mo	0.14±0.1	0.12±0.03	0.06±0.03	0.02±0.02
Fe	83.57±1.2	88.28±2.2	21.31±3.5	0

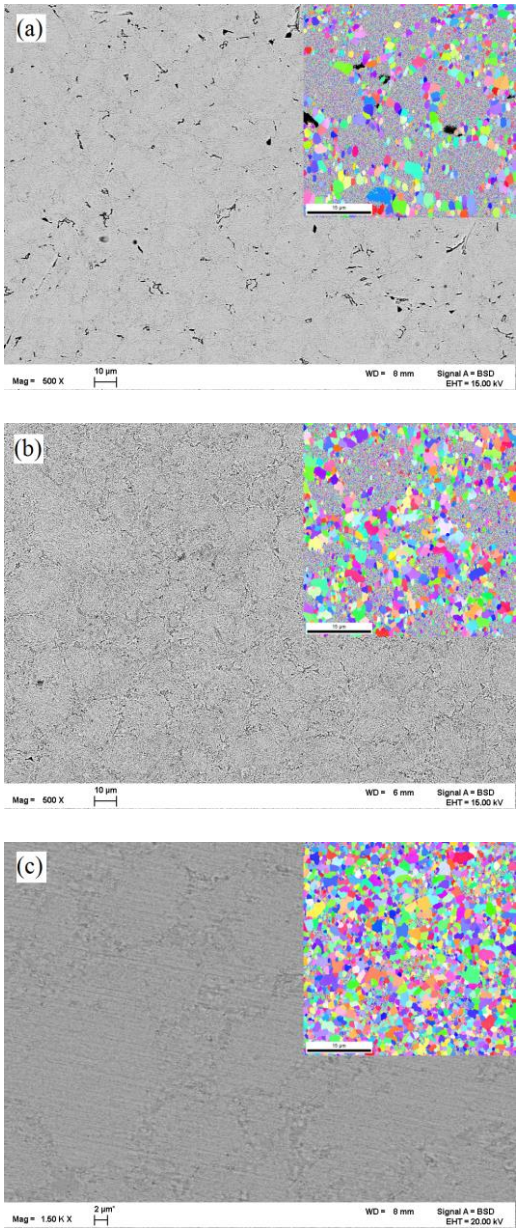

Fig. 1. SEM and EBSD micrographs of the 14LMT specimens SPSed at (a) 850 ºC, (b) 950 ºC and (c) 1050 ºC for 45 min.

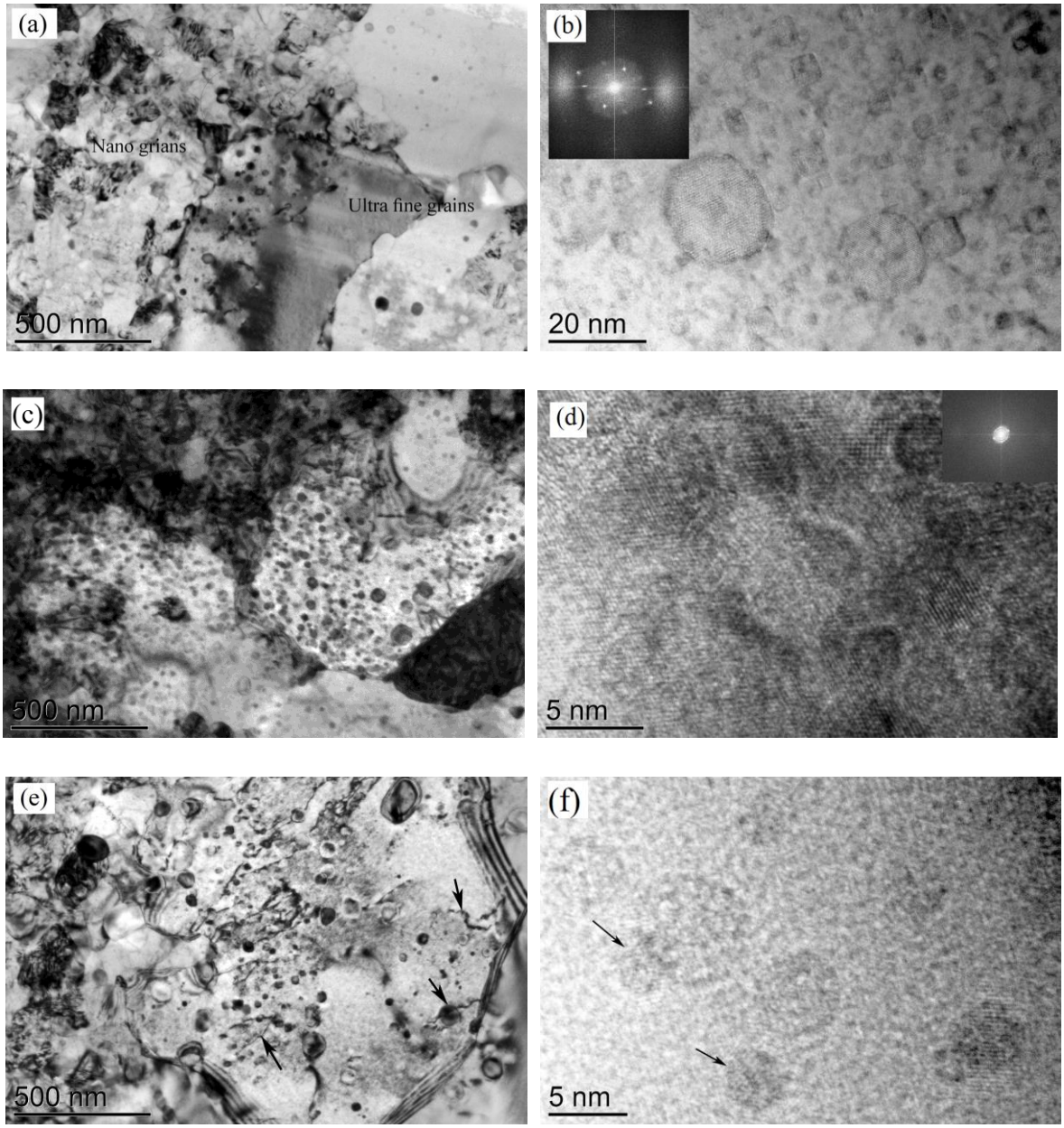

Fig. 2. TEM micrographs of 14LMT alloy SPSed at 850 ºC for 45 min: (a) a bright field micrograph of a bimodal grain size distribution, and (b) nanoparticles with diameters varying between 3-20 nm. TEM images of 14LMT alloy SPSed at 850 ºC for 45 min: (c) a bright field micrograph of a bimodal grain size distribution, and (d) HRTEM micrograph showing nanoparticles smaller than 5 nm. TEM micrographs of the 14LMT SPSed at 1050 ºC for 45 min: (e) a bright field image showing interaction of nanoparticles and dislocations in the grain interior, and (f) a HRTEM micrograph of the nanofeatures indicated by arrows.

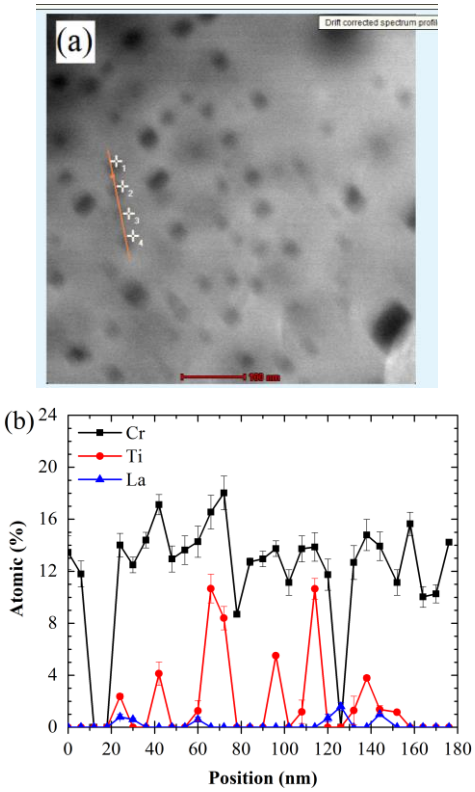

Fig. 3. (a) STEM HAADF micrograph of four particles with faceted morphology and (b) the concentration profile for (a) as a function of position in a 14LMT specimen (sintered at 950 ^{o}C for 45 min).

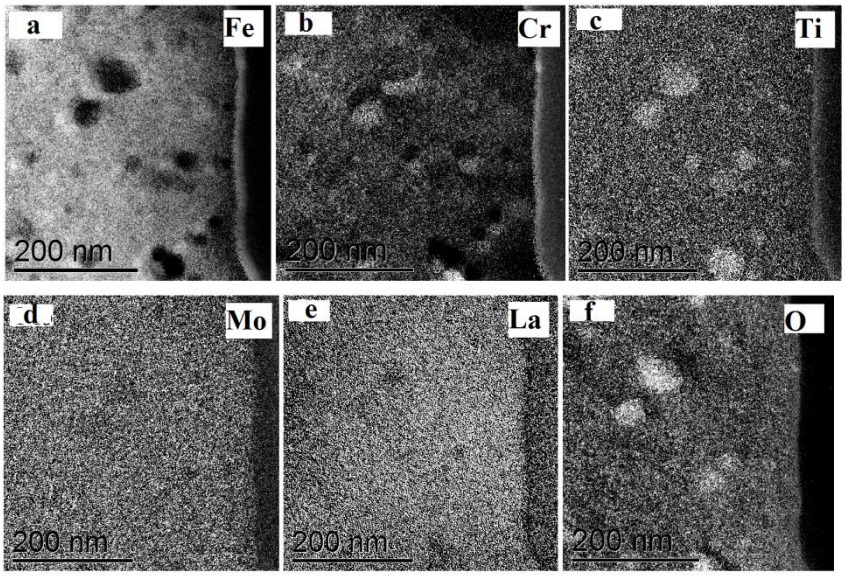

Fig. 4. EFTEM elemental maps showing (a) Fe, (b) Cr, (c) Ti, (d) Mo, (e) La and (f) O in 14LMT alloy SPSed at 950 ^{o}C for 45 min.

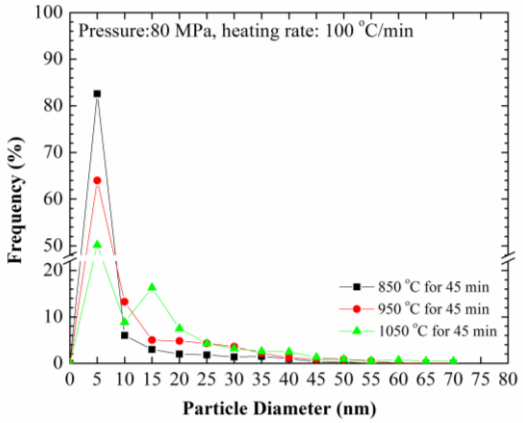

Fig. 5. Particle size distribution plots of 14LMT alloy after SPS at 850, 950 and 1050 °C for 45 min.

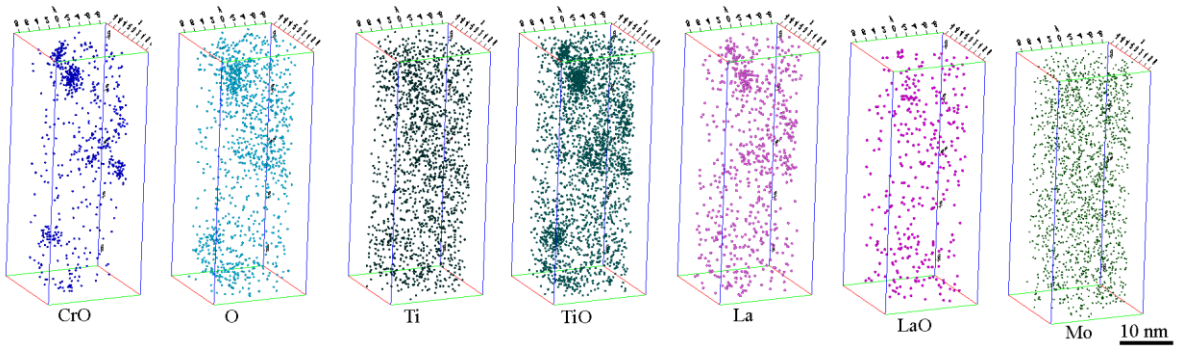

Fig. 6. Three dimensional (3-D) APT reconstruction maps of the 14LMT alloy after SPS at 950 ^{o}C for 45 min.

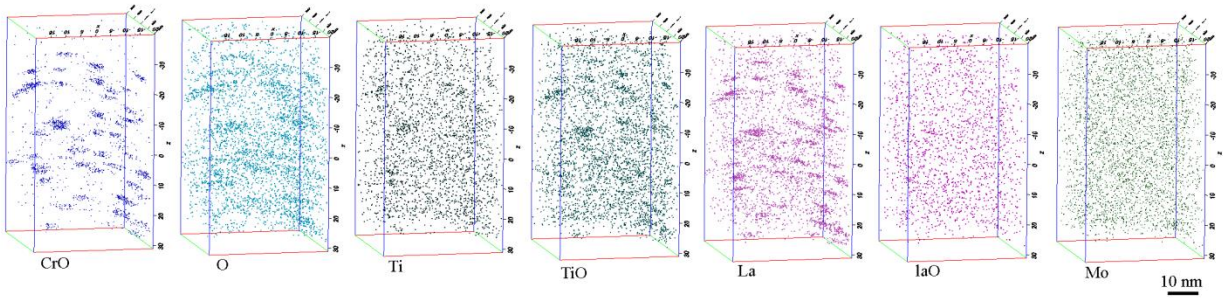

Fig. 7. Three dimensional (3-D) reconstruction maps of APT data showing clustering of CrO, TiO and La from the 14LMT alloy after SPS at 1050 ^{o}C for 45 min.

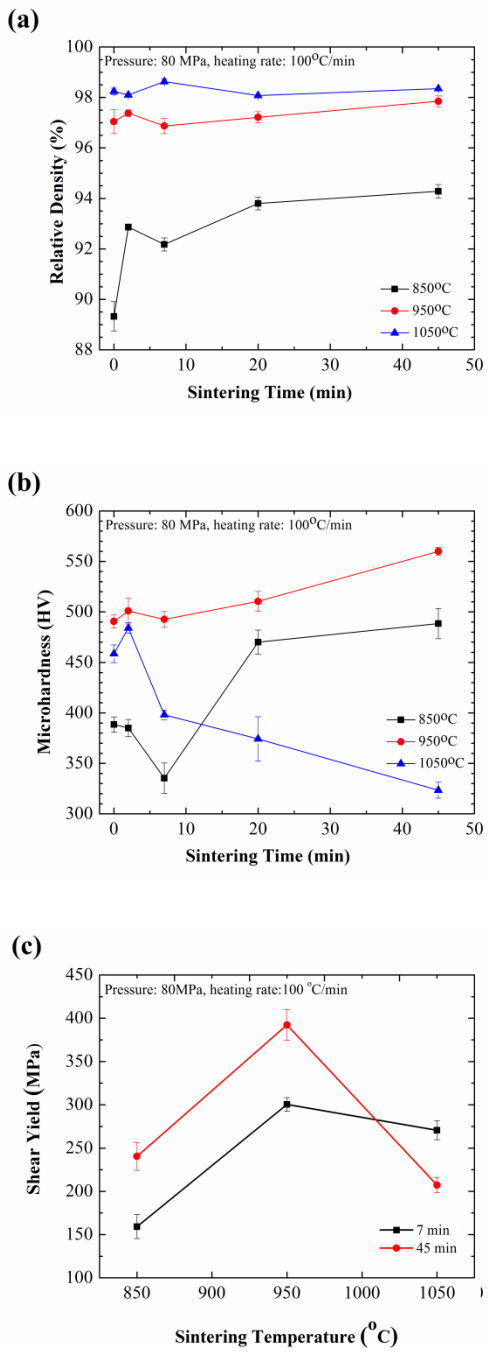

Fig. 8. (a) The relative density, (b) microhardness and (c) shear yield stress of 14LMT alloy SPSed at three different SPS temperatures for two different sintering dwell times.